RESEARCH ARTICLE

EcoMat
FUNCTIONAL MATERIALS FOR GREEN ENERGY AND ENVIRONMENT

WILEY

Self-powered virtual olfactory generation system based on bionic fibrous membrane and electrostatic field accelerated evaporation

Peng Yang[1,2] | Yuxiang Shi[1,2] | Xinglin Tao[1,2] | Zhaoqi Liu[1,2] |
Shuyao Li[1,2] | Xiangyu Chen[1,2] 🔟 | Zhong Lin Wang[1,2,3] 🔟

[1]CAS Center for Excellence in Nanoscience, Beijing Institute of Nanoenergy and Nanosystems, Chinese Academy of Sciences, Beijing, China

[2]School of Nanoscience and Technology, University of Chinese Academy of Sciences, Beijing, China

[3]School of Materials Science and Engineering, Georgia Institute of Technology, Atlanta, Georgia, USA

Correspondence
Xiangyu Chen and Zhong Lin Wang, CAS Center for Excellence in Nanoscience, Beijing Institute of Nanoenergy and Nanosystems, Chinese Academy of Sciences, 100083 Beijing, China.
Email: chenxiangyu@binn.cas.cn (X. C.) and zhong.wang@mse.gatech.edu (Z. L. W.)

Funding information
Beijing Nova Program, Grant/Award Number: Z201100006820063; National Key R&D Project from Minister of Science and Technology, Grant/Award Number: 2021YFA1201601; National Natural Science Foundation of China, Grant/Award Number: 62174014; Youth Innovation Promotion Association of the Chinese Academy of Sciences, Grant/Award Number: 2021165

Abstract

Olfactory plays an important role in virtual reality technology. In this work, a bionic fibrous membrane (BFM) integrated with the function of electrostatic field accelerated evaporation (EFAE) is applied for realizing the virtual olfactory generation (VOG) system. The BFM is capable of self-driven unidirectional liquid transmission and EFAE process is induced on BFM by using an ultrafast voltage-elevation triboelectric nanogenerator (UVE-TENG). The output voltage from UVE-TENG can reach 8 kV within 40 ms, which is enough to maintain all of the functions of VOG system. Meanwhile, the output current from UVE-TENG is smaller than 1 μA, leading to a safe and human compatible system. The flow rate of the volatile liquid spray from the system emitter can reach 0.1 μl/s, and the average evaporation rate of the BFM device with integrated EFAE function is 0.12 mg/s. Accordingly, the user of this VOG system can feel the generation of odor within 3 s, while the switching of different odor channels can be wirelessly controlled by a mobile phone. This VOG system enhances the user's immersive and interactive experience for virtual reality technology. The similar system composed of UVE-TENG, reed switch, BFM and EFAE devices also has potential application value in assisted breathing treatment and nasal delivery.

KEYWORDS
bionic fibrous membrane, electrostatic field accelerated evaporation, self-powered, virtual olfactory

1 | INTRODUCTION

Virtual reality (VR) and augmented reality (AR) technology constructs a communication channel between the real world and the metaverse, giving users an immersive, interactive, and imaginative simulation experience.[1–3] In order to recreate a complete virtual environment, olfactory is also an inevitable element. Compared with visual and auditory perception, olfactory generation has many unique requirements, such as high sensitivity, inertia, repeatability,

and individual differences.[4–7] Adding an olfactory simulator to the traditional audio-visual virtual environment not only enhance the authenticity of the immersion experience, but also provide an additional method to manipulate people's emotion and memory.[8–11] On the other hand, as a typical self-powered device, triboelectric nanogenerator (TENG) has excellent controllability, portability, and safety, which can be widely used in all kinds of human wearable devices.[12–21] The combination study of TENG and VR/AR equipment has also drawn notable attention, where TENG can serve as the sensory element or the energy module for the VR/AR system. In the past 2 year, a series of applications of TENG device as the somatosensory interaction interface,[22–24] virtual tactile stimulator,[25–27] and manipulator of virtual objects[28–30] have been rapidly reported. Therefore, TENG technique may also provide a different approach for promoting the development of virtual olfactory technology.

Typically, there are four types of odor generation methods for virtual olfactory devices: free emission,[31] card-based heating,[32] surface acoustic wave atomization,[33] and gas injection.[34] However, these methods all have their own limitations, such as the slow response speed of the free emission, the poor compatibility of the card-based heating system, the high working noise of acoustic atomization device, and the large size of gas injection apparatus. Alternatively, Electrospray (ES) is a liquid atomization technology similar as acoustic atomization, which may also satisfy the purpose of odor generation. However, the ES device usually requires high-voltage power source and its safety is challenging for the human-wearable applications.[35–41] In this case, considering the high-voltage and low-current characteristics of TENG, it provides an opportunity to establish a safe and effective human-wearable ES device. It is worth noting that high-voltage also has a benign effect on the evaporation of water. The introduction of the high electric field effectively reduces the free energy barrier of water evaporation and increases the flux of evaporated water molecules.[42–47] Accordingly, the odor can be carried by the mist droplets and diffusion rapidly with the ultrafast evaporation of the droplets. Therefore, the TENG can be used as a special power source to control the rapid ejection and fast evaporation of volatile liquids, which may realize a different approach for the virtual olfactory technology.
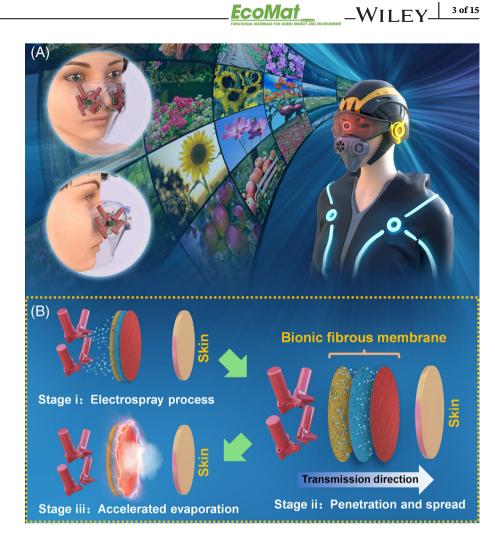
In this work, a self-powered virtual olfactory generation (VOG) system is realized based on an ultrafast voltage-elevation TENG (UVE-TENG) with charge accumulation principle, which can precisely control the generation, mixing and diffusion of different odor. The core element of the system is a bionic fibrous membrane (BFM) with the functions of unidirectional liquid transmission and electrostatic field accelerated evaporation

(EFAE). The output voltage from UVE-TENG almost instantly reaches few thousand volts and the related output current is still at microampere level, which is enough to drive the VOG and also maintain its safety to human skin. This VOG system has two operation chambers separated by a BFM, where the ES devices are in the front chamber and the EFAE process is occurred in the back chamber. By applying different perfume solution to ES device, the VOG system can provide diversified olfactory information interacting between virtual environment and users. Hence, this VOG system can undertake the olfactory interaction for various VR/AR system and it is also expected to be used for intelligent medical treatment and gas mask.

2 | RESULTS

2.1 | The overall design and working mechanism of the VOG system

In order to establish the interactive experience between virtual environment and users, the VOG system is integrated into a wearable mask, as shown in Figure 1A. The mask completely covers the nose area of the human face to ensure that the generated odors can enter the user's nasal cavity smoothly. The mask contains two groups of odor generating devices, which are located on both sides of the nasal dorsum. At the same time, the odor generating devices are not in contact with the nose, to ensure the wearing comfort of the mask and minimize the impact on the normal physiological activities of the human body. Each group of odor generating devices includes four ES units targeting at a BFM as the liquid receiver. The BFM is fabricated by electrospinning method to improve the efficiency of mist droplet phase transition. Compared with the traditional single-layer quick drying materials, the prepared BFM have excellent characteristics such as rapid absorption of droplets and self-driven unidirectional water transmission. Then, a spherical electrode is placed on the skin surface of the nose, in order to guide the EFAE process. The whole device is driven by the high-electrostatic field from UVE-TENG, while the generation, mixing and diffusion of odor can be precisely adjusted by the multi-channel switch module. Two operation chambers separated by BFM receiver are designed for VOG system and the generated gas molecules finally enter the human nasal cavity through three stages, as shown in Figure 1B. The ES process happens in the front chamber, where the perfume solution firstly accumulates at the emitter tip owing to the wicking effect and then, is sprayed onto the receiver under the action of high-voltage electrostatic field. Due to the surface energy

FIGURE 1 The concept and working mechanism of VOG system. (A) Schematic diagram of the application scenario of the VOG system in VR/AR, showing the wearing effect and internal structure of the VOG system. (B) Operation mechanism of the VOG system, including (i) the ES process between the emitter and receiver, (ii) the penetration and spread of the sprayed droplets on the BFM, and (iii) the EFAE between the receiver and the nose.
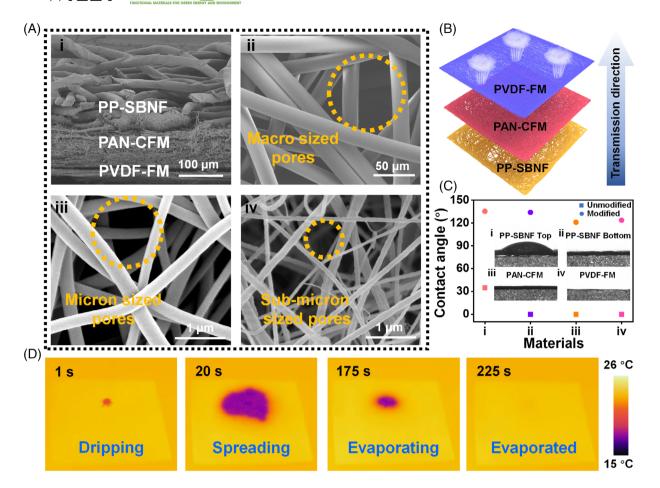

difference of each side of the BFM receiver, the perfume solution quickly penetrates and spreads on the BFM. After that, in the back chamber, the perfume solution on the BFM evaporates rapidly under the drive of EFAE process and then, the generated odor can be quickly received by the human nose at the exit of back chamber, leading to the virtual olfactory experience. The double chamber structure can also effectively block the natural emission process of odor from the emitter, leading to a highly controllable generation process of different odor.

2.2 | Penetration and spreading of the liquid in the BFM

As shown in Figure 1B, two operation chambers of the VOG system are separated by a BFM film. The BFM is capable of self-driven unidirectional liquid transmission and it is composed of three layers of different fiber membranes, which are polypropylene spun-bond non-woven fabric (PP-SBNF), polyacrylonitrile-based carbon fiber membrane (PAN-CFM) and polyvinylidene fluoride fiber membrane (PVDF-FM), respectively (see Figure 2A

[i]). The preparation process of the BFM is shown in Figure S1 and explained in detail in the methods section, while the surface SEM images of three fiber membranes are exhibited in Figure 2A (ii–iv). The distribution of pore size of three fiber membranes are designed to follow Murray's law. The PP-SBNF has an average fiber diameter of 20 μm and an average pore size of 100 μm (macro-sized pores), which are bigger than PAN-CFM (micron-sized pores, average fiber diameter is 250 nm and average pore size is 1.5 μm) and PVDF-FM (sub-micron-sized pores, average fiber diameter is 120 nm and average pore size is 700 nm). Further, the wider range of SEM images of the material surface are shown in Figure S2 to show the distribution of pores in different fiber membranes. Figure 2B illustrates the spatial arrangement of different materials in the BFM. It is important to note that PAN-CFM is a conductive film and thus, BFM can also serve as the electrode during ES and EFAE process. Equally notable is that according to the Laplace equation, narrower pores and a higher degree of super wettability can increase the capillary force to enhance the penetration and spreading of liquid in capillary pores. Therefore, in order to achieve unidirectional liquid transmission, the

FIGURE 2 Design and characterization of BFM. (A) SEM image of BFM with three-layer structure. (i) The cross-sectional images of BFM. (ii–iv) SEM images of PP-SBNF (ii), PAN-CFM (iii), PVDF-FM (iv). (B) Schematic diagram of BFM. The direction of the arrow indicates the transmission direction of the droplet on the BFM. (C) Contact angle of fiber membranes before and after hydrophilic treatment, (i-iv) contact angle images of PP-SBNF top (i), PP-SBNF bottom (ii), PAN-CFM (iii) and PVDF-FM (iv) after hydrophilic treatment. (D) Infrared thermal images on BFM during water evaporation (droplet volume: 15 μl), when the temperature returns to the ambient temperature, the water is considered to be completely evaporated.

surface energy gradients of three fiber membranes are further modified, as described in the methods section. The contact angle change of the three fiber membranes before and after hydrophilic treatment is shown in Figure 2C and Figure S3. Then, the transmission process of water in three modified monolayer fiber membranes is tested, as depicted in Figure S4. The experimental result indicated that droplet (volume: 15 μl) spread in different degrees on each fiber membrane surface with a certain degree of penetration. This process is mainly dominated by the Laplace pressure between the fiber membranes. On the other hand, the spreading area of the same volume of water on PP-SBNF, PAN-CFM, and PVDF-FM gradually increases, as described in Figure S5, suggesting that the pore size of capillary channels has a pivotal influence on water spread. The photos of BFM prepared from the three-layer fiber membrane are illustrated in

Figure S6. When the water is on the top side of BFM, owing to the surface energy difference between each layer of fiber membrane, it quickly penetrates from PP-SBNF to PVDF-FM as well as forming spreading simultaneously, and the spreading area enlarges with the increase of the volume of water (Figure S7). Combining the above discussion, the transmission procedure of liquid inside BFM can be analyzed in the vertical and horizontal directions. In the vertical direction, since the gradual reduction of pore size, the pressure difference between the upper and lower ends can be analyzed by the conical model, as shown in Figure S8(A). According to the Laplace equation, the capillary pressure difference between PP-SBNF and PAN-CFM (ΔP_1) can be expressed as:

$$\Delta P_1 = \frac{4\gamma \cdot \cos\theta_2}{D_{PP-SBNF}} - \frac{4\gamma \cdot \cos\theta_1}{D_{PAN-CFM}}, \quad (1)$$
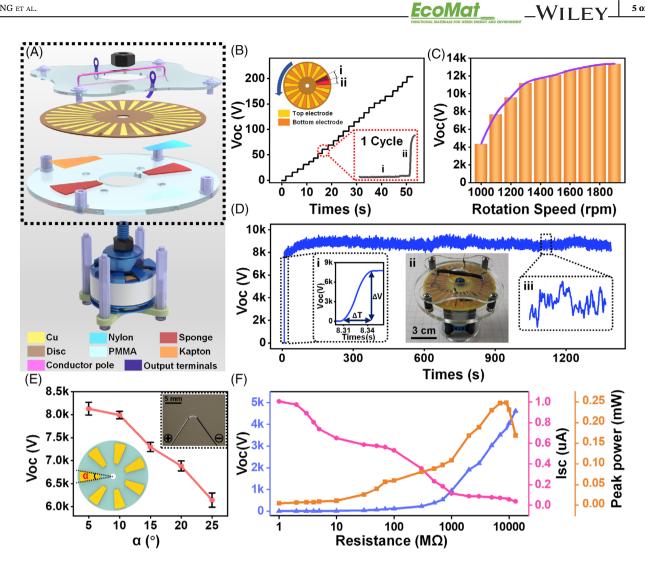
FIGURE 3 The structure and electrical characteristics of the UVE-TENG. (A) Structural diagram of UVE-TENG. (B) The open-circuit voltage output during the counterclockwise step rotation of the disc. Upper left inset: diagrammatic sketch of disc rotation. Lower right illustration: voltage output curve of one cycle, which is divided into voltage holding stage (i) and voltage rise stage (ii). (C) Open-circuit voltage output by UVE-TENG under different disc rotating speed. (D) UVE-TENG output stability test (the disc speed: 1200 rpm). (i) Startup characteristics of UVE-TENG. (ii) The photograph of UVE-TENG. Scale bar: 3 cm. (iii) Detail drawing of UVE-TENG output waveform. (E) Response of UVE-TENG open-circuit voltage to the electrode center angle (disc speed is 1200 rpm). Lower left inset: schematic diagram of circle center angle of sector electrode. Upper right illustration: image of discharge between spherical electrodes driven by UVE-TENG. Scale bar: 5 mm. (F) Dependence of output voltage, current and peak power on different resistive loads.

where θ_1 and θ_2 are the contact angle of PP-SBNF and PAN-CFM respectively, $D_{PP-SBNF}$ and $D_{PAN-CFM}$ are the pore diameters of the two fiber membranes, γ is the water surface tension coefficient. At room temperature, the ΔP_1 between PP-SBNF and PAN-CFM is 0.19 MPa, and similarly, the ΔP_2 between PAN-CFM and PVDF-FM interface is 0.22 MPa, indicating that the water transport in the vertical direction is an unidirectional transmission process. In addition, owing to the horizontal Laplace pressure, water can spread rapidly along the fiber channel in the horizontal direction, as shown in Figure S8(B) (see Movie S1). Compared with PP-SBNF and PAN-CFM, PVDF-FM have higher permeation and

diffusion driving force for liquid as well as larger specific surface area, indicating a faster water evaporation rate (Figure S9).Therefore, the BFM prepared by selecting three kinds of film arrangements can effectively improve the response speed of the device through the action of Laplace pressure. In order to characterize the water evaporation on the BFM, the infrared camera is used for detecting the temperature change of the BFM (Figure 2D). The water droplet (volume: 15 μl) drops upon the BFM and the whole evaporation process takes 225 s with an evaporation of 0.07 mg/s (ambient temperature: 20 °C, wind scale: 0), showing the quick-drying characteristics of the BFM.
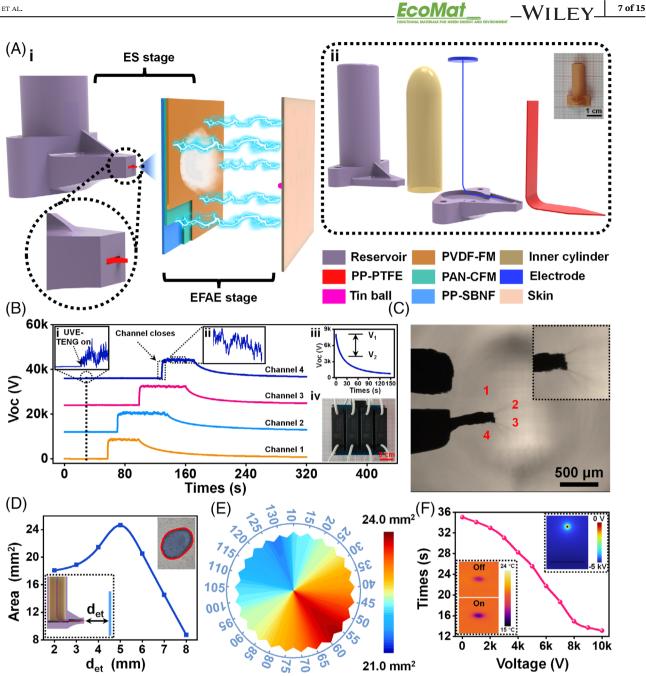
2.3 | Configuration and output performance of the UVE-TENG

As the energy source of the VOG system, the structure of UVE-TENG is illustrated in Figure 3A. The power generation part is mainly composed of triboelectric films with opposite electrification polarity (Kapton and Nylon), double-sided disc electrodes, conductor pole, and output terminals. Polymethylmethacrylate (PMMA) acts as the supporting component to ensure structural stability during operation. The top and bottom of the disc are arranged 30 sector electrodes with a central angle of 5° (top and bottom electrodes), which are driven by a brushless motor for high-speed operation. It is worth noting that the electrodes on both sides are not completely coincident in space, but there is a certain angle dislocation. The conductor pole and output terminals locate above the top electrode and keep effective contact with the top electrode array to continuously transfer and transmit charges. The sponge lays under the triboelectric films to ensure full contact between the bottom electrode of the disc and the triboelectric films. When the disc rotates clockwise, the bottom electrode array of the disc slides relative to Kapton and Nylon. Due to the triboelectric electrification and charge transfer between the dielectric layers and the electrodes, the surface charge density of the dielectric layer remains saturated. Simultaneously, the angular dislocation exists between the top and bottom electrodes, so there is not much effect between the charges on the top and bottom electrodes. On this basis, electrodes A and B are selected as research objects to explore the voltage output mechanism of UVE-TENG, as depicted in Figure S10. According to the contact electrification principle and charge transfer characteristics, the electrification process of UVE-TENG can be divided into four stages. In stage i, the disc rotates clockwise and the electrodes A and B do not enter the area where the dielectric layers are located. At this time, the electrodes A and B are not in contact with the conductor pole and the UVE-TENG has no voltage output. In stage ii, electrodes A and B rotate above Nylon and Kapton respectively, and negative and positive charges are induced on electrodes A and B respectively owing to electrostatic induction. At this moment, there is directional movement of charges on the conductor pole to keep electrostatic balance. When in stage iii, the conductor pole locates in the gap between the top electrodes and the charges on electrodes A and B continue to maintain. Similarly, new induced charges accumulate in the subsequent electrodes. Then, in stage iv, with the continuous rotation of the disc, surfaces of the electrodes A and B contact the output terminals, and their surface charges are output outward to generate current in the external circuit. Therefore,

neglecting charge leakage, the output voltage of UVE-TENG ($V_{OC}(t)$) can be expressed by the following equation:

$$V_{OC}(t) = 2NfqR_{air}\left(1 - e^{-\frac{t}{R_{air}C_A}}\right), \qquad (2)$$

where N is the number of sector electrodes in the top electrode array, f is the rotation frequency of the disc, t is the rotation time, q is the amount of charge on a single sector electrode, C_A is the capacitance between two output terminals, and R_{air} is the air resistance air resistance between output terminals (The detailed deduction process of the above equation is displayed in note S1). Hence, the UVE-TENG output voltage increases with the amount of accumulated charges, but there is a saturation process due to the charge leakage phenomenon. When the charge generation and leakage reach a balance, the output voltage maintain a relatively stable output state. Figure 3B shows the voltage output curve of UVE-TENG during step rotation, where the output voltage appears a step-by-step elevation (see Figure S11). With the rotation of the TENG, the output terminals alternately pass through the top electrodes and two stages of output signal are periodically presented, which are voltage holding (i) and voltage rising (ii). The experimental results in Figure 3C show that the output voltage of UVE-TENG increase with the rise of rotating speed (the output voltage of UVE-TENG can reach 13.38 kV at 1900 rpm). However, when the rotating speed increases, the charge leakage of top electrode becomes more serious. Thus, the output voltage may reach a saturated value based on the dynamic balance of charge accumulation and charge leakage. The longtime running test of UVE-TENG are illustrated in Figure 3D, where the speed of brushless motor is controlled to 1200 rpm (the output voltage is 8 kV). The output voltage of UVE-TENG remains stable after 1400 s test time. The scanning electron microscopic (SEM) images of the two dielectric films before and after the test are shown in Figure S12. It can be seen from Figure 3D (i) that the voltage output of UVE-TENG increases rapidly to about 8 kV within 40 ms, indicating its instantaneous response capability. Similarly, when the disc stops rotating, the voltage output curve of UVE-TENG is illustrated in Figure S13. Further, the impact of the center angle of the sector electrode on the voltage output is also discussed, as shown in Figure 3E. With the center angle increases, the charge transfer frequency decreases rapidly, resulting in the decrease of output voltage. Figure 3F shows the change of open-circuit voltage and short-circuit current of UVE-TENG with external resistance. It can be seen that the power curve of the load shows a trend of first increase and then decrease, which

FIGURE 4 The structure analysis, operation process and parameter control of ES and EFAE devices. (A) Working principle of single ES and EFAE devices. (i) Schematic diagram of ES and EFAE devices operation process. (ii) Structure representation of the components of the ES device. Inset: the photograph of the assembled ES device. Scale bar: 1 cm. (B) Four channels control of the output voltage of UVE-TENG (the disc speed: 1200 rpm). (i) Comparison of the voltage waveform before and after UVE-TENG startup with the reed switch opens. (ii) Detail drawing of the voltage waveform after the reed switch closes. (iii) After the reed switch opens, the falling curve of UVE-TENG output voltage. (iv) Physical picture of the multi-channel switching module, scale bar: 3 cm. (C) Jet photo at the emitter tip, 4 jets appear at the same time (driving voltage: 5 kV). Inset: detail drawing of the tip. (D) Response of the spray area on the receiver to the distance (d_{et}) between the emitter tip and the receiver. Lower left illustration: schematic diagram of the d_{et}, and the sectional view of the ES device shows the internal structure after assembly. Upper right inset: photograph of a receiver sprayed with blue ink. (E) Dependence of the spray area on the angle of the emitter tip. (F) The time required for the water (volume: 2 μl) on the receiver to evaporate completely under different electrostatic voltages. The series voltage divider is used to obtain the low voltage output of UVE-TENG. Lower left inset: infrared thermal imaging comparison on the receiver with the high-voltage electrostatic field off and on. Upper right illustration: Simulation of voltage distribution between receiver and spherical electrode.

is consistent with the volt-ampere characteristic curve of the resistance property. Meantime, the output current is always below 1 μA, indicating the high safety for the human involving applications. When the matching resistance is 9 GΩ, the maximum peak power of 0.25 mW can be obtained.

2.4 | Design and implementation of ES and EFAE devices

The ES and EFAE processes of odor solutions occurs in the front and back chambers respectively and the whole working process is shown in Figure 4A (i). As illustrated in Figure 4A (ii) the ES device is consisted of a shell manufactured by resin 3D printing, an inner cylinder and a polypropylene (PP)-polytetrafluoroethylene (PTFE)-based emitter, while the PAN-CFM inside BFM works as the receiver electrode. The inner cylinder can store 0.2 ml of the perfume solution each time (Figure S14, the detailed preparation process is explained in methods section). To realize the electronic control of multiple ES emitters, a wireless multi-channel switching module based on high-voltage electrostatic management is designed (Figures 4B, S15, and S16), adapting the reed switch as the basic control unit. The reed switch is a passive electronic switching element with contactors, which uses inert gas to seal two elastic reeds in a glass tube. When the external magnetic field acts around the glass tube, the two reeds in the tube are magnetized and attract each other, and the contactors on the reeds are pulled in to switch on the circuit. After the external magnetic field disappears, the two reeds are separated due to their elasticity to disconnect the line. The controllable switching voltage of the reed switch used in this work can reach 20 kV, which is enough to work with the output signal from UVE-TENG. Furthermore, the opening and closing of the external magnetic field of the reed switch are controlled by WIFI wireless communication and thus, a communication interface for regulating the ES processes is realized based on cloud communication platform and intelligent mobile devices. The on–off control test of the multi-channel switching module for the voltage output of the UVE-TENG is illustrated in Figure 4B. Here, the output signal from UVE-TENG can be well managed by the reed switches and the enlarged curve of the output signal can be seen from Figure 4B (i–iii). When the reed switch closes, the measured voltage rises rapidly to 7.5 kV (channel 2) within 0.661 s. Then, after the reed switch opens, the measured voltage drops from 8 kV to 4 kV within 15 s, and finally dropped to 0 V after a period of time.

In the process of ES, the emitter plays a decisive role in the spraying and atomization of the liquid. Hence, based on the microfluidic technology of porous media, a PP-PTFE-based emitter is applied to this work (Figures S17, S18), which is composed of PP coarse skeleton covered by PTFE fibers. The liquid flow rate of the emitter can be explored by the capillary model of porous media. According to the Washburn equation,[48] the

moving speed (ϑ_L) of the liquid-front on PP-PTFE-based emitter can be expressed as:

$$\vartheta_L = \frac{1}{4} \cdot \sqrt{\frac{D_h^2}{D_c} \cdot \frac{\gamma \cdot \cos(\theta)}{\mu t}}, \qquad (3)$$

where γ is the liquid surface tension, θ is the contact angle, μ is the liquid viscosity, D_c is the capillary pore diameter, D_h is the hydraulic pore diameter, t is the time (see note S2 for the derivation process). Further, the volumetric flow rate on the emitter can be expressed as:

$$Q_L = \frac{1}{4} A\alpha \cdot \sqrt{\frac{D_h^2}{D_c} \cdot \frac{\gamma \cdot \cos(\theta)}{\mu t}}, \qquad (4)$$

where A, the cross-sectional area of the emitter, α, the ratio of capillary channel area to cross-sectional area. It can be found that the volumetric flow rate on the emitter is related to the shape and liquid properties of the emitter. Through the wicking experiment of the rectangular emitter (long: 35 mm, wide: 3 mm, and thick: 0.15 mm), the average volumetric flow rate of the perfume solution in PP-PTFE-based emitter is 0.21 µl/s. Therefore, in this work, the volume flow at each cross-section of the emitter tip (Q_{L_i}) can be expressed as:

$$Q_{L_i} = \frac{s_i}{s} \cdot Q_L, \qquad (5)$$

where s is the width of the emitter (3 mm) and s_i is the width of each cross-section. Usually, the liquid forms a Taylor cone at the capillary port under the combined action of surface tension and electric field. However, the electric field produced by UVE-TENG is quite high and the Taylor cone is no longer stable, resulting in the trickle ejected from the cone tip. Then, the repulsion between the same kind of charges decomposes the trickle into smaller mist droplets. It should be noted that there is a turn-on voltage (V_{ON}) in the process of ES,[49] which can be expressed as:

$$V_{ON} = \sqrt{\frac{D_c \gamma \cos(\theta)}{4\varepsilon_0}} \cdot \ln\left(\frac{4s_{er}}{D_c}\right), \qquad (6)$$

where D_c is the capillary pore diameter, s_{er} is the distance from the emitter tip to the receiver, γ is the liquid surface tension, ε_0 is the dielectric constant of air, θ is the degree of Taylor cone half angle (49.3°). On the other hand, UVE-TENG voltage management can be realized by adjusting the disc rotation frequency. Hence, according

to equation (1), the minimum rotation frequency of disc (f_{min}) can be expressed as:

$$f_{min} = \frac{V_{ON}}{2NqR_{air}\left(1 - e^{-\frac{t}{R_{air}C_A}}\right)}, \quad (7)$$

In this work, the distance between the electrode end and the capillary emitter tip is still a certain distance. Therefore, when the distance between the emitter tip and the receiver is 5 mm, the turn-on voltage of the ES is at least 4 kV. At this time, the image of ES driven by UVE-TENG is illustrated in Figure 4C (see Movie S2) and it can be seen that the ejected stream has four branch at the same time (see Movie S3), due to the randomly distributed microchannels inside the PP-PTFE emitter. Combined with Equations (4) and (5) above, the initial droplet diameter of ES can be expressed as:

$$r_e = \left(\frac{\rho}{4\pi^2\gamma \cdot \tan\left(\frac{\pi}{2}-\theta\right) \cdot \left[\left(\frac{V_A}{V_{ON}}\right)^2 - 1\right]}\right)^{\frac{1}{3}} \cdot (Q_t)^{\frac{2}{3}}, \quad (8)$$

where ρ is the density of the liquid, θ is the degree of Taylor cone half angle (49.3°), γ is the liquid surface tension. The V_A and V_{ON} are the actual operating voltage and the ES turn-on voltage respectively. Q_t is the volumetric flow rate at the emitter tip and the initial droplet size can be obtained at the micron scale. Here, the final spray area of the receiver is determined by using an evaluation index (colored dyes are added to the perfume solution in this process). When the output voltage of UVE-TENG is 8 kV, the impact of the distance between the emitter tip and the BFM receiver is shown in Figure 4D and the influence of voltage on the spray area are illustrated in Figure S19(A). The rising of voltage can increase the liquid volume emitted by ES, while the excessive increase of voltage may lead to the discharge between the emitter and the receiver. Similarly, the change of the area on the receiver with time is shown in Figure S19(B), from which it can be seen that the sprayed volume of the emitter tip is about 1 μl within 10 s (the ejection flow is 0.1 μl/s on average). The angle of the emitter tip also has a certain impact on the final spray area (Figure 4E), which is rather a minor effect. Meanwhile, in order to meet the spatial layout requirements of VOG system, the effect of the rotation angle of the single ES device on the spray area is verified, as depicted in Figure S20. The EFAE process is occurred in the back chamber between the BFM receiver and the spherical electrode (diameter: 0.5 mm) pasted around the nasal cavity. During the EFAE process,

the high-voltage electrostatic field can reduce the free energy of phase transition and improve the evaporation efficiency (see Movie S4). The effect of high-voltage electrostatic field on the perfume solution evaporation can be quantified from the perspective of molecular dynamics. According to the activated Arrhenius expression, the effect of high-voltage electrostatic field on the perfume solution evaporation can be expressed as:

$$J = Ae^{\left(-\frac{E_a - \alpha|E|}{k_B T}\right)}, \quad (9)$$

where J is the evaporation flux of solution molecules, A is the system reference constant, k_B is the Boltzmann constant, T is the ambient temperature during evaporation, E_a is the free energy during liquid evaporation, α is the parameters related to the high-voltage electrostatic field, and E is the electric field intensity. Obviously, the effect of EFAE is affected by the voltage at both ends of the device and the distance between two electrodes. The rising of voltage shortens evaporation time of the perfume solution on the BFM receiver (Figures 4F, S21). When the high-voltage electrostatic field is applied, the temperature of the central part of the liquid on the infrared image drops significantly, indicating that the liquids are gathered in this area and evaporated rapidly. Compared with the control group, the high-voltage electrostatic field also has a certain inhibitory effect on the spreading of liquid, which is due to the liquid accumulation caused by electrostatic field. The increase of the distance between the BFM and the spherical electrode could weaken the enhancement effect on the perfume solution evaporation (Figure S22). Then, with the increase of the liquid volume on the receiver, the evaporation time gradually gets longer (Figure S23). When the electrostatic voltage is 5 kV and the distance between electrodes is 5 mm, the perfume solution evaporation rate can reach up to 0.12 mg/s (ambient temperature: 20°C, wind scale: 0), which is 70% higher than the evaporation rate without electrostatic field. The relationship between the odor intensity perceived by the human body and its concentration conforms to the Stenvens's power law[50]:

$$I = k \cdot c_g^n, \quad (10)$$

where I is the odor intensity perceived by the human olfactory, c_g is the concentration of the spice volatilized to the air at the sniffer, k is the relative sensitivity of the human olfactory to the odor, and n is the intensity index. The concentration of aroma in the nasal cavity can be analyzed by the double-membrane mass transfer model. To simplify the model, the perfume solution is regarded

as an ideal solution with low solute concentration and water as the main solvent. Then the concentration of solute in the air inhaled by the human nasal cavity c_n can be expressed as:

$$c_n = \frac{Ss\beta}{4\pi d^2 \vartheta} \cdot \varepsilon c_0 e^{-\frac{\varepsilon St}{V}}, \tag{11}$$

where S is the area of the gas–liquid two-phase interface, s is the maximum cross-sectional area of the nasal cavity, β is the inspiratory time, d is the distance between the nasal cavity and the BFM, ϑ is the single inspiratory volume of the human body, ε is a parameter related to the properties of the perfume solution, c_0 is the initial concentration of the solute, t is the volatilization time and V is the volume of the perfume solution on the BFM (see note S3 for the specific derivation process). Hence, whether people can finally perceive odor is related to various factors including the nature of the odor itself and the solute concentration. In the current experiment, we mainly focus on the application of representative top-note perfumes for the VOG system. The perfumes of the top notes are usually volatile liquids with short residence time and fresh smell and therefore, it is easy to control and switch the odor in the ES and EFAE devices by using top-note perfumes. Lemon perfume belongs to the citrus olfactory family and it is a typical top-note perfume solution with high odor identification. Here, a perfume solution with lemon odor is applied to study the human perception of the aroma sprayed by the ES and EFAE device, where 15 volunteers are selected for the test (Figure S24, see the Methods section for the test method) and the sprayed volume from the emitter tip is about 1 μl. In this work, the olfactory responses of volunteers are tested according to the relevant standards of the Chinese Smell Recognition Test (CSIT) and a lemon perfume solution with 1 wt% is finally selected as the test solvent (Figure S25, see note S4 for the experiment methods, and Tables S1, S2, S3, S4, S5, S6, S7, S8, S9, S10 show the statistical results). In the single-channel spray experiment, after the EFAE is turned on, the subjects feel the presence of the aroma in about 3.1 s on average. At the same time, the subjects generally cannot feel the aroma after 5.16 s, which is caused by the complete evaporation of the perfume solution on the receiver.

2.5 | Multi-channel verification and system application

Figure 5A shows the diversified applications of this VOG technique consisting of UVE-TENG, reed switch, BFM and EFAE devices. In addition to odor generation, the similar system is also expected to play a vital role in assisted breathing treatment and nasal delivery. Even though its operation voltage is few thousands volts, this VOG system still has superior human-friendly characteristics due to the low output current from UVE-TENG, which allow it to be integrated into various masks. The wearing performance and detailed structure of the mask are shown in Figures S26 and S27, respectively. The spray processes of multi-channel ES driven by UVE-TENG is demonstrated in Figure 5B (distance between the emitter tip and the receiver is 5 mm), which proves the stability of the 4-channels operation. Meanwhile, it can be seen that with the rising of driving voltage, the spray area also increases accordingly, which verifies the controllability of the injection volume of the liquids through UVE-TENG voltage. Furthermore, in the high-voltage electrostatic field, the variation of the spray area with the distance between the emitter tip and the receiver is illustrated in Figure 5C. It can be seen that the ES result has an optimal distance, which is about 6 mm with rotation speed of 1300 rpm of UVE-TENG. Furthermore, UVE-TENG can respectively drive different emitters through channel switching (Figure 5D), which confirms the reliability of UVE-TENG. On the other hand, the liquid evaporation effect of the four areas on the receiver in the multi-channel working mode is tested (Figure 5E). Since the spatial position of the spherical electrode on the outer surface of the nasal cavity is not completely symmetrical relative to the four areas, the evaporation time of the liquid on the four areas is different. The wireless controlling process of the 4-channel ES by mobile devices is illustrated in Figure 5F. When the mobile phone interface is set in the sequence of channel 1, 2, 3, 4, the liquid carried by each channel sequentially appears on the receiver, and the response speed of ES is related to the WIFI signal intensity and transmission distance. Similarly, the 2-channel ES process diagram is shown in Figure S28. Figure 5G illustrates the evaporation process of the liquid on the BFM receiver with the help of high-voltage electrostatic field, and the liquid spread on a single channel evaporates completely after 5 s (ambient temperature: 20 °C, wind scale: 0), confirming the rapid evaporation characteristics (see Movie S5). The interaction performance between the VOG system and the user is further tested (Figure S29), and the results indicate that during the operation of the entire system, the users can feel the change of odor on each channel in about 3 s on average. The integrated design of BFM and EFAE ensures that the odor can be released quickly, indicating the great potential of the VOG system in practical application.
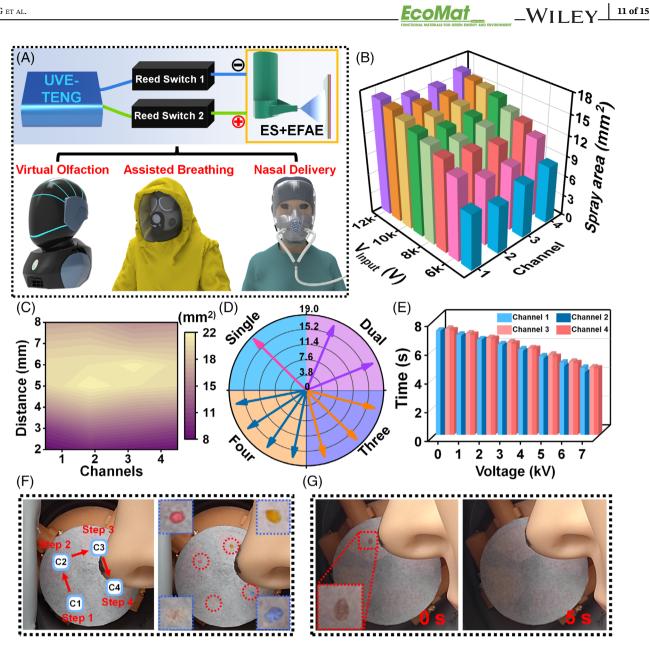
FIGURE 5 Verification and experiment of multi-channel ES and EFAE devices. (A) Application scenario of basic units composed of UVE-TENG, reed switch, ES and EFAE devices. (B) Response of the spray area of the receiver on each channel to the UVE-TENG output voltage (the distance between the emitter tip and the receiver is 8 mm). (C) Dependence of the spray area on the receiver on the distance between the emitter tip and the receiver. (D) Driving state of UVE-TENG for different number of ES devices (UVE-TENG voltage: 8 kV). (E) Images of ES in the mask through mobile phone control. (F) Photos of EFAE process for a single channel on the receiver in the mask.

3 | DISCUSSION

In summary, an integration of a VOG system into a wearable mask is proposed and investigated, in which the high-voltage electrostatic field generated by UVE-TENG serves as the power source. The double chamber structure is applied for VOG system separated by BFM, while the ES and EFAE occur in the front and back chambers respectively. The porous media based on PP-PTFE is used as the emitter in the ES device and the spray flow rate of the perfume solution can reach 0.1 μl/s on average under

the drive of high electrostatic field. A BFM based on Murray's law is fabricated as receiver, which is composed of PP-SBNF, PAN-CFM, and PVDF-FM, and the pore size distribution of these fiber films are respectively in the scale of macro-, micron-, and sub-micron-. The sprayed droplets penetrate and spread rapidly on the BFM due to the Laplace pressure and the water evaporation rate on the BFM can reach 0.07 mg/s at ambient temperature of 20°C. Further, the EFAE rate of perfume solution reaches up to 0.12 mg/s with the output voltage of 5 kV from UVE-TENG. When lemon perfume, a typical top-note

perfume, is selected as the test solution, the users can feel the change of the generated odor in the back chamber within about 3 s during the operation of the VOG system. A 4-channels ES device is also applied for the VOG system, where the changing-over of different odor channels can be wirelessly controlled by a mobile phone. The output voltage from UVE-TENG can reach 8 kV within 40 ms, while its output current is at microampere scale. Hence, for the first time, the ES and EFAE devices can be safely integrated into wearable mask, leading to a human compatible system. The proposed VOG system provides a different approach for improving the immersive and interactive experience of VR/AR users, which can strength the communication between the virtual digital world and the real world. Moreover, the similar system composed of UVE-TENG, BFM and EFAE devices also can be applied for many different purposes, including the assisted breathing treatment, nasal delivery and so on.

4 | METHODS

4.1 | Fabrication of BFM

First, 5 g fatty alcohol polyoxyethylene ether (Model TF629C, Transfar) was added into 495 g deionized water and stirred with a magnetic stirrer (Model HJ4A, Xinrui) for 30 min to prepare the solution. A certain quality of polyvinylidene fluoride (PVDF) powder (Arkema) was dissolved in the mixed solution of N, N-Dimethyl Acetamide (Aladdin) and acetone (Xilong-Scientific) (The volume ratio is 2:3), and stirred for 5 h under the condition of water bath heating at 50 °C to prepare PVDF solution (20 wt%). Then, PVDF-FM was spun on PAN-CFM (SJ-Technol) surface by electrospinning technology (Microinjection pump: Model TYD01-01, Leadfluid). PAN-CFM was fixed on the aluminum flat receiver, and adjusted to the spinning voltage was 13 kV, the collection distance was 15 cm, and the flow rate was 5 μl/min to prepare double fiber membrane. After spinning, removing the double fiber membranes and soaking it in fatty alcohol polyoxyethylene ether solution for 15 min, and then, taking it out and drying under vacuum in a drying oven at 77 °C for 6 h. One side of the PP-SBNF (Jingtai) was tightly covered by a layer of adhesive tape. The masked fabric was placed into a plasma cleaner (Model IoN 40, PVA TePla) for cleaning (cleaning power: 150 W, time: 5 min). After plasma treatment, the tape mask was peeled off from one side of the fabric. The side of PP-SBNF not covered by adhesive tape was sprayed with granular glue (Model Super 77, 3 M) to ensure its adhesion, and then the adhesive side of PP-SBNF was pasted on the surface of PAN-CFM in the double fiber membranes to obtain the BFM.

4.2 | Preparation of an ES unit

The three-dimensional structure of the reservoir was designed by software (Solidworks 2017, Dassault Systèmes) and manufactured by 3D printing (Model D133, Creality). The inner cylinder (Model BI-EP002, BioFount) was located inside the reservoir, which was made of PP. The PP-PTFE-based emitter was shape cut by a laser cutting machine (Model LM-1390, LaserMen), the cutting power was 10 W, the moving speed of the laser head was 200 mm/s, and the distance between the laser head and the object to be cut was 7 mm. The emitter entered the inner cylinder from the circular opening and extended to the bottom of the inner cylinder, while the emitter tip was reserved outside the reservoir to realize the ES. The electrode entered the inner cylinder through the reservoir and fixed them together. At the same time, there was still a certain distance between the electrode end and the emitter tip to avoid discharge.

4.3 | Fabrication of the perfume solution

As a typical top-note perfume, lemon perfume was mainly composed of D-limonene, and its olfactory threshold was 200 ppb, which had the advantages of fast volatility and high odor identification. First, 5 g hydrosoluble perfume (Lemon RuiBo) was added into 495 g of deionized water, and stirred for 1 h under the water bath heating condition at 30°C. After the stirring was completed, sealing the beaker containing the solution and letting it stand for 2 h at room temperature to obtain the perfume solution of 1 wt%. Perfume solutions of other mass fractions used in typical top-note perfumes response test are also manufactured according to this procedure.

4.4 | Device fragrance test method for subjects

A total of 15 (mean age 27.71 years) non-smokers with birthplaces across mainland China participated in the main study. They reported to have no respiratory allergy or upper respiratory infection at the time of testing. Written informed consent and consent to publish was obtained from participants in accordance with ethical standards of the Declaration of Helsinki (1964). These volunteers participated in the previous olfactory response test according to the relevant standards of the Chinese

Smell Identification Test (CSIT) to prove the normality of the volunteers' olfactory response and the sensitivity to the lemon perfume used in the test. The experimental is carried out at room temperature and windless environment to reduce the influence of the test environment on odor. In single-channel ES experiment, spherical electrodes were first attached to the subject's nasal dorsum. The electrodes attached to the back of the nose did not affect the olfactory receptors inside the subject's nasal cavity. Then, the mask was worn on the subject's face and ensured that there was no direct contact between the receiver and the nose. With an elastic sling as a means to connect the mask and the face, this ensures the tightness of the mask and face fit. The ES device was turned off after working 5 s, and the electrostatic field between the receiver and the human body was turned on. Furthermore, the moments when the subjects perceived the aroma and when they could not perceive the aroma were recorded. In multi-channel ES experiments, the test method was the same as that of single-channel ES experiments, but it should be noted that each time after completing a channel test, it was necessary to wait 2 min to relieve the fatigue of nasal receptors, and then continue to next channel test.

4.5 | Fabrication of mask integrated with VOG system

The half-mask was used as the main structure, while the flanks, mounting brackets, and receiver supports were designed with software (Solidworks 2017, Dassault Systèmes), and the product was fabricated by 3D printing (Model D133, Creality). The rotary locking structure was introduced to connect the main body with other components as well as the quick-release design was adopted on the mounting frame to ensure quick replace of reservoirs.

4.6 | Experiment measurement and characterization

A programmable electrometer (Model 6514, Keithley) was used to test the transferred charge of UVE-TENG. The voltage output signal of the UVE-TENG was measured with an electrostatic voltmeter (Model 341B, Advanced Energy Industries). The speed tester (Model 6236P, Victor) was used to record the rotating speed of the disc. The external load of UVE-TENG was simulated by resistance box (Model MC-21-B, MingCheng) to test its optimal peak power. The charge and voltage signals were collected and recorded by the signal acquisition card (Model USB-6356, National Instrument), and a software platform for real-time acquisition, analysis, and

processing of experimental data was built based on Lab-VIEW (2017, National Instrument). The on–off test of the reed switch was performed with digital multimeter (Model 86B, Victor), and record the signal with a computer terminal. The temperature change on the BFM during evaporation was observed by the infrared camera (Model 225 s, Fotric). The contact angles of the three fiber membranes (PP-SBNF, PAN-CFM, PVDF-FM) before and after modification were measured by a contact angle meter (Model CA100C, Innuo). The weight change during wicking of the porous media-based emitter was reflected by an electronic balance (BSA224S-CW, Sartorius) to derive the volumetric flow rate of liquid on the emitter. Ink drop flight test equipment (Dropwatcher, JexXpert) was used to photograph the ES process at the emitter tip in the high-voltage electrostatic field. SEM (Nanosem 450, Nova) was used to study the micro morphology of BFM, PP-PTFE- based emitter and two dielectric films in UVE-TENG.

4.7 | Experiments with human subjects

We have studied the olfactory perception of sprayed perfume of seven different subjects. The experiments with these human subjects have been performed in compliance with all the ethical regulations under a protocol that was approved by the Institutional Review Board at Beijing Institute of Nanoenergy and Nanosystems, Chinese Academy of Sciences. The participants in the odor and device tests were the authors of the paper and some popular volunteers. All of us gave written, informed consent about the experimental procedure.

CONFLICT OF INTEREST

The authors declare no conflict of interest.

ORCID

Xiangyu Chen https://orcid.org/0000-0002-0711-0275
Zhong Lin Wang https://orcid.org/0000-0002-5530-0380

REFERENCES

1. Huang K-H, Rupprecht P, Frank T, Kawakami K, Bouwmeester T, Friedrich RW. A virtual reality system to analyze neural activity and behavior in adult zebrafish. *Nat Methods*. 2020;17(3):343-351. doi: 10.1038/s41592-020-0759-2

2. Mishra S, Kim Y-S, Intarasirisawat J, et al. Soft, wireless periocular wearable electronics for real-time detection of eye vergence in a virtual reality toward mobile eye therapies. *Sci Adv* 2020;6(11): eaay1729. doi: 10.1126/sciadv.aay1729

3. Yu X, Xie Z, Yu Y, et al. Skin-integrated wireless haptic interfaces for virtual and augmented reality. *Nature*. 2019; 575(7783):473-479. doi: 10.1038/s41586-019-1687-0

4. Bushdid C, Magnasco MO, Vosshall LB, Keller A. Humans can discriminate more than 1 trillion olfactory stimuli. *Science* 2014;343(6177):1370–1372. doi: 10.1126/science.1249168

5. Keller A, Gerkin RC, Guan Y, et al. Predicting human olfactory perception from chemical features of odor molecules. *Science* 2017;355(6327):820–826. doi: 10.1126/science.aal2014

6. Lapid H, Shushan S, Plotkin A, et al. Neural activity at the human olfactory epithelium reflects olfactory perception. *Nat Neurosci*. 2011;14(11):1455-1461. doi: 10.1038/nn.2926

7. Rosenberg B, Misra TN, Switzer R. Mechanism of olfactory transduction. *Nature*. 1968;217(5127):423-427. doi: 10.1038/217423a0

8. Kamrava SK, Tavakol Z, Talebi A, et al. A study of depression, partnership and sexual satisfaction in patients with post-traumatic olfactory disorders. *Sci Rep*. 2021;11(1):20218. doi: 10.1038/s41598-021-99627-9

9. Liu M, Zhang Y, Wang J, et al. A star-nose-like tactile-olfactory bionic sensing array for robust object recognition in non-visual environments. *Nat Commun*. 2022;13(1):79. doi: 10.1038/s41467-021-27672-z

10. Radvansky BA, Dombeck DA. An olfactory virtual reality system for mice. *Nat Commun*. 2018;9(1):839. doi: 10.1038/s41467-018-03262-4

11. Zou L-q, Yang Z-y, Wang Y, et al. What does the nose know? Olfactory function predicts social network size in human. *Sci Rep*. 2016;6(1):25026. doi: 10.1038/srep25026

12. Chen B, Yang N, Jiang Q, Chen W, Yang Y. Transparent triboelectric nanogenerator-induced high voltage pulsed electric field for a self-powered handheld printer. *Nano Energy*. 2018; 44:468-475. doi: 10.1016/j.nanoen.2017.12.026

13. Lei R, Shi Y, Ding Y, et al. Sustainable high-voltage source based on triboelectric nanogenerator with a charge accumulation strategy. *Energ Environ Sci*. 2020;13(7):2178-2190. doi: 10.1039/D0EE01236J

14. Liu Y, Liu W, Wang Z, et al. Quantifying contact status and the air-breakdown model of charge-excitation triboelectric nanogenerators to maximize charge density. *Nat Commun*. 2020; 11(1):1599. doi: 10.1038/s41467-020-15368-9

15. Luo J, Gao W, Wang ZL. The triboelectric Nanogenerator as an innovative technology toward intelligent sports. *Adv Mater*. 2021;33(17):2004178. doi: 10.1002/adma.202004178

16. Karan SK, Maiti S, Lee JH, Mishra YK, Khatua BB, Kim JK. Recent advances in self-powered tribo-/piezoelectric energy harvesters: all-in-one package for future smart technologies. *Adv Funct Mater*. 2020;30(48):2004446. doi:10.1002/adfm.202004446.

17. Mahapatra SD, Mohapatra PC, Aria AI, et al. Piezoelectric materials for energy harvesting and sensing applications: roadmap for future smart materials. *Adv Sci*. 2021;8(17):2100864. doi:10.1002/advs.202100864.

18. Luo J, Wang ZL. Recent progress of triboelectric nanogenerators: from fundamental theory to practical applications. *EcoMat*. 2020;2(4):e12059. doi: 10.1002/eom2.12059

19. Lu Y, Tian H, Cheng J, et al. Decoding lip language using triboelectric sensors with deep learning. *Nat Commun*. 2022;13(1): 1401. doi: 10.1038/s41467-022-29083-0

20. Guo H, Pu X, Chen J, et al. A highly sensitive, self-powered triboelectric auditory sensor for social robotics and hearing aids. *Sci Robot* 2018;3(20):eaat2516. doi: 10.1126/scirobotics.aat2516

21. Yang P, Shi Y, Li S, et al. Monitoring the degree of comfort of shoes In-motion using triboelectric pressure sensors with an Ultrawide detection range. *ACS Nano*. 2022;16(3):4654-4665. doi: 10.1021/acsnano.1c11321

22. Shi Q, Qiu C, He T, et al. Triboelectric single-electrode-output control interface using patterned grid electrode. *Nano Energy*. 2019;60:545-556. doi: 10.1016/j.nanoen.2019.03.090

23. Wen F, Sun Z, He T, et al. Machine learning glove using self-powered conductive Superhydrophobic triboelectric textile for gesture recognition in VR/AR applications. *Adv Sci*. 2020;7(14): 2000261. doi: 10.1002/advs.202000261

24. Zhang W, Deng L, Yang L, et al. Multilanguage-handwriting self-powered recognition based on triboelectric nanogenerator enabled machine learning. *Nano Energy*. 2020;77:105174. doi: 10.1016/j.nanoen.2020.105174

25. Liu Y, Wang L, Zhao L, et al. Thin, skin-integrated, stretchable triboelectric Nanogenerators for tactile sensing. *Adv Electron Mater*. 2020;6(1):1901174. doi: 10.1002/aelm.201901174

26. Shi Y, Wang F, Tian J, et al. Self-powered electro-tactile system for virtual tactile experiences. *Sci Adv*. 2021;7(6):eabe2943. doi: 10.1126/sciadv.abe2943

27. Yao G, Xu L, Cheng X, et al. Bioinspired triboelectric Nanogenerators as self-powered electronic skin for robotic tactile sensing. *Adv Funct Mater*. 2020;30(6):1907312. doi: 10.1002/adfm.201907312

28. Chen T, Shi Q, Zhu M, et al. Triboelectric self-powered wearable flexible patch as 3D motion control Interface for robotic manipulator. *ACS Nano*. 2018;12(11):11561-11571. doi: 10.1021/acsnano.8b06747

29. Chen T, Zhao M, Shi Q, et al. Novel augmented reality interface using a self-powered triboelectric based virtual reality 3D-control sensor. *Nano Energy.* 2018;51:162-172. doi: 10.1016/j.nanoen.2018.06.022

30. He T, Sun Z, Shi Q, et al. Self-powered glove-based intuitive interface for diversified control applications in real/cyber space. *Nano Energy.* 2019;58:641-651. doi: 10.1016/j.nanoen.2019.01.091

31. Kaye JJ. Making scents: aromatic output for HCI. *Interactions.* 2004;11(1):48-61. doi: 10.1145/962342.964333

32. Kim DW, Cho YH, Nishimoto K, Kawakami Y, Kunifuji S, Ando H. Development of Aroma-Card Based Soundless Olfactory Display 2009:703–706.

33. Itou S, Iseki M, Kato S, Nakamoto T. Olfactory and visual presentation using olfactory display using SAW atomizer and solenoid valves. Presented at: proceedings of the 23rd international conference on intelligent user interfaces companion; 2018; Tokyo, Japan. doi: 10.1145/3180308.3180331

34. Yanagida Y, Noma H, Tetsutani N, Tomono A. An unencumbering, localized olfactory display. Presented at: CHI '03 extended abstracts on human factors in computing systems; 2003; Ft. Lauderdale, Florida, USA 10.1145/765891.766109

35. Chen D-R, Pui DYH, Kaufman SL. Electrospraying of conducting liquids for monodisperse aerosol generation in the 4 nm to 1.8 μm diameter range. *J Aerosol Sci.* 1995;26(6):963-977. doi: 10.1016/0021-8502(95)00027-A

36. Tang K, Gomez A. On the structure of an electrostatic spray of monodisperse droplets. *Phys Fluids.* 1994;6(7):2317-2332. doi: 10.1063/1.868182

37. Zhao X-Y, Li C, Yang W, Deng W. Paper-based electrospray emitters. *J Aerosol Sci.* 2017;113:108-113. doi: 10.1016/j.jaerosci.2017.07.013

38. Ouyang J. Application of intrinsically conducting polymers in flexible electronics. *SmartMat.* 2021;2(3):263-285. doi: 10.1002/smm2.1059

39. Nguyen TC, Choi W-S. Electrospray mechanism for quantum dot thin-film formation using an electrohydrodynamic jet and light-emitting device application. *Sci Rep.* 2020;10(1):11075. doi: 10.1038/s41598-020-67867-w

40. Taylor G. Disintegration of water drops in an electric field. *Proc R Soc Lond A Math Phys Sci.* 1964;280(1382):383-397.

41. Xie J, Jiang J, Davoodi P, Srinivasan MP, Wang C-H. Electrohydrodynamic atomization: a two-decade effort to produce and process micro−/nanoparticulate materials. *Chem Eng Sci.* 2015;125:32-57. doi: 10.1016/j.ces.2014.08.061

42. Asakawa Y. Promotion and retardation of heat transfer by electric fields. *Nature.* 1976;261(5557):220-221. doi: 10.1038/261220a0

43. Fei J, Ding B, Koh SW, et al. Mechanistic investigation of electrostatic field-enhanced water evaporation. *Adv Sci.* 2021;8(18):2100875. doi: 10.1002/advs.202100875

44. Okuno Y, Minagawa M, Matsumoto H, Tanioka A. Simulation study on the influence of an electric field on water evaporation. *J Mol Struct.* 2009;904(1):83-90. doi: 10.1016/j.theochem.2009.02.035

45. Sun CQ. Water electrification: principles and applications. *Adv Colloid Interface Sci.* 2020;282:102188. doi: 10.1016/j.cis.2020.102188

46. Takano K, Tanasawa I, Nishio S. Active enhancement of evaporation of a liquid drop on a hot solid surface using a static electric field. *Int J Heat Mass Transfer.* 1994;37:65-71. doi: 10.1016/0017-9310(94)90010-8

47. Zhang H-H, Wang B-B, Xu Z-M, Li X-C, Yan W-M. Molecular dynamics simulation on evaporation enhancement of water and aqueous nano-films by the application of alternating electric field. *Int J Heat Mass Transfer.* 2019;145:118735. doi: 10.1016/j.ijheatmasstransfer.2019.118735

48. Masoodi R, Pillai KM. Darcy's law-based model for wicking in paper-like swelling porous media. *AlChE J.* 2010;56(9):2257-2267. doi: 10.1002/aic.12163

49. Wampler FM, Blades AT, Kebarle P. Negative ion electrospray mass spectrometry of nucleotides: ionization from water solution with SF6 discharge suppression. *J Am Soc Mass Spectrom.* 1993;4(4):289-295. doi: 10.1016/1044-0305(93)85050-8

50. Theimer ET. *Fragrance Chemistry: the Science of the Sense of Smell.* Elsevier; 2012.

SUPPORTING INFORMATION

Additional supporting information can be found online in the Supporting Information section at the end of this article.